Comprehensive Exam Report

The Maxwell Semiconductor Bloch Equations in one and two dimensions

Samuel McLaren

April 3, 2019

Abstract

Vertical External Cavity Surface Emitting Lasers (VECSELs) are modern powerhouses in terms of current technological improvements. The current state-of-the-art in numerically modeling these lasers involves the coupling of Maxwell's wave equations to the Semiconductor Bloch Equations (MSBE). We discuss previous work with these equations, specifically strategies devised for ultra-short pulse generation. This includes, optimizing the chip coating and QW structure designs, pumping levels, and output coupling and absorber characteristics. We also briefly discuss some hysteresis. We proceed to discuss the transverse Maxwell Semiconductor Bloch Equation (tMSBE) model, it's basic modifications and preliminary results, along with some desired goals for the future. This includes generalizing to arbitrary cavity geometries and non-normal incidences, modulating our gain region to study PT symmetry within a VECSEL, implementing intensity and temperature dependence within the refractive indices of our gain chip to study Kerr and thermal lensing effects with regards to self-mode-locking, and general characterizations of higher order mode generation and pulse instabilities through the manipulation of transverse pumping schemes. In addition, we hope to do a full numerical study of the SBE with regards to appropriate numerical solvers as well as to compile a manual for proper usage of the MSBE model.

Contents

List of Figures

1 Background

1.1 Motivation

Over the past two decades, Vertical External Cavity Surface Emitting Lasers (VECSELs) have proven to be highly versatile in producing ultrafast high power pulses with compact and varying geometries [1,3–10]. For a more thorough review of the progress, and accomplishments, of these lasers, see Rahini-Imam [11] or Guina et al [12]. VECSELs, as ultrafast pulse generators, show promise for their versatility in terms of wave-length, ease of manufacturing and stability, and capability for producing pulses with high peak and average powers, variable repetition rates, and ultrafast pulse lengths. Rate based models exist and are well studied for various cavity geometries [13]. However, these models rely on many fitted parameters, including a prescribed gain curve, to give an accurate description of the resulting modelocked pulse. This limits the predictive capabilities of the models as well as its ability to accurately model the non-equilibrium gain effects. In many situations this is not ideal, and a different approach must be used [14]. In order to properly model them, one needs to look at the microscopic many-body effects of the gain structure, [6]. The Maxwell Semiconductor Bloch Equation (MSBE) model does just that by coupling wave propagation to a polarization source term using the most advanced semiconductor model available. A generic full cavity computational domain is shown in Figure 1 [1].

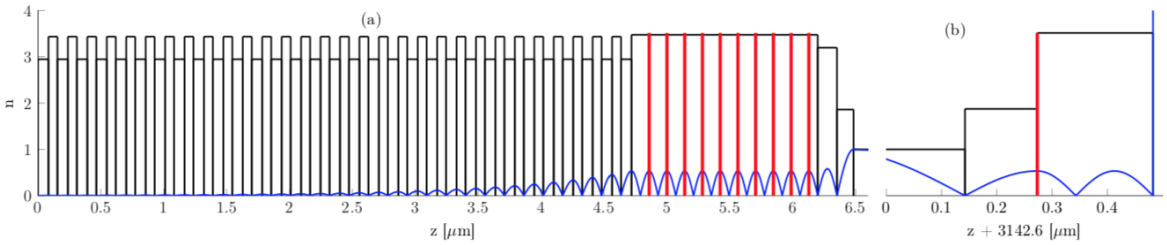

Figure 1: Computational domain with (a) gain chip and (b)SESAM separated by large air gap [1]

In black is the material refractive index showing the various components of the cavity with the underlying fundamental standing wave for the resonator cavity in blue. From left to right, we have our Distributed Bragg

Reflector (DBR) which consists of many pairs of selectively chosen material layers whose refractive indices provide a gradual, broadband reflection of the incoming field [15]. From there, were have our active region. Our quantum wells, the red lines, are where we have gain in our system. This is where we must compute our polarization source term, using our Semiconductor Bloch Equations (SBE) to be discussed shortly. We then have an antireflective (AR) coating to compensate for dispersion and allow the pulse to seamlessly travel into and out of the gain region. From there we have a large air gap which is by far the largest component of our computational domain. We then have our absorber structure (SESAM), consisting of another AR coating, a low density quantum well that acts as a passive modelocking device, and then an output coupler that allows a small portion of the light to escape the cavity.

2 Underlying Model

The two primary components of the model are the electric field propagation using Maxwell's wave equation and the active region simulation using the Semiconductor Bloch Equations [16], which describe the carriers, electrons and holes, as well as the microscopic polarization states through a coupled set of Optical Bloch Equations with added nonlinearities which arise from many-body interactions. The propagation of the electric field within the cavity is modeled using Maxwell's wave equation, [17]

$$\left[\frac{\partial^2}{\partial z^2} - \frac{n_b^2}{c_0^2}\frac{\partial^2}{\partial t^2}\right] E(z,t) = \mu_0 \frac{\partial^2}{\partial t^2} P(z,t). \tag{1}$$

wherein, our electric field is E, our source polarization is P and n_b, c_0, μ_0 are the material refractive index, vacuum speed of light, and vacuum permittivity respectively. This is used to propagate within individual material components throughout the cavity, including the large air cavity. We assume that all materials are linearly dispersive for simplicity, and tune our spatial and temporal step sizes so that a single spatial step is the exact distance traveled by light within the medium in a single time step. Through this process, our pulse will merely translate from one time-space step to another, at least within a single medium. However, when our pulse approaches an interface, boundary conditions for Maxwell's equations give us an appropriate trans-

fer matrix that relates the incoming and outgoing electric fields. Note that we assume our quantum wells, our polarization sources, are narrow relative to cavity components and thus act only at the interfaces between particular materials. Thus, inside a given medium, we do not have any induced polarization. For the interface between components $j, j+1$ with forward (backward) moving fields expressed by $+(-)$ respectively and refractive indices n_j, n_{j+1}, our electric field transfer matrix becomes

$$(n_j + n_{j+1}) \begin{bmatrix} E_{j+1}^+ \\ E_j^- \end{bmatrix} = \begin{bmatrix} 2n_j & n_{j+1} - n_j \\ n_j - n_{j+1} & 2n_{j+1} \end{bmatrix} \begin{bmatrix} E_j^+ \\ E_{j+1}^- \end{bmatrix} - \mu_0 c_0 \frac{\partial}{\partial t} P(z,t). \quad (2)$$

for our vacuum permeability, μ_0, where whenever we are crossing over a quantum well, we will have a nonzero polarization [14]. In order to compute the polarization response present when at a quantum well interface, we note that our macroscopic polarization is a sum over momentum space for our quantum polarizations,

$$P(t) = \sum_k d_{cv} p_k(t). \quad (3)$$

We model this microscopic polarization using the Semiconductor Bloch Equations (SBE), [16] a coupled system of Optical Bloch Equations with nonlinear many body effects,

$$\begin{aligned} \frac{\partial}{\partial t} p_k &= -i\omega_k p_k - i\Omega_k (n_k^e + n_k^h - 1) + \Gamma_{deph} + \Lambda_{spont}^p + \frac{\partial}{\partial t} p_k \mid_{scatt}; \\ \frac{\partial}{\partial t} n_k^{e(h)} &= i \left[\Omega_k p_k^* - \Omega_k^* p_k \right] + \Gamma_{scatt} + \Lambda_{spont}^n + \Gamma_{fill} + \frac{\partial}{\partial t} n_k^{e(h)} \mid_{scatt}; \end{aligned} \quad (4)$$

Therein, $n_k^{e(h)}$ is the occupation number for electrons (holes) in state k. Note the population inversion, $n_k^e + n_k^h - 1$. It is this quantity which most readily indicates the growth of various modes through the burning of kinetic holes in momentum states [14]. When this population inversion is positive (negative) our system will exhibit gain (absorption). As the carriers are depleted in a certain spectral region we get inversion *bleaching* which will no longer exhibit gain (absorption). The polarization dephasing is modeled using a phenomenological decay rate derived from simulations using scattering approximations on the Second Borne-Markov level [18].

$$\Gamma_{deph} = -\frac{1}{\tau_{deph}} p_k. \quad (5)$$

Although simulations for the scattering and dephasing terms have been run on the Second Borne-Markov level [19], this is extremely computationally demanding, requiring multi-dimensional matrix sums at each step. So much so that it becomes intractable for optimizing cavity design and is useful only in investigating new structures and confirming particularly interesting results. We instead use phenomenologically fit parameters for the dephasing of the interband polarization. Similarly, the occupation numbers, $n_k^{e(h)}$ and pumping are modeled using an exponential recovery to a background Fermi distribution, $f_k^{e(h)}$

$$\Gamma_{scatt} = -\frac{1}{\tau_{scatt}} \left(n_k^{e(h)} - f_k^{e(h)} \right). \tag{6}$$

The kinetic hole filling is modeled through a similar process,

$$\Gamma_{fill} = -\frac{1}{\tau_{fill}} \left(n_k^{e(h)} - F_k^{e(h)} \right). \tag{7}$$

where $F_k^{e(h)}$ are dynamically computed based on the current total density and temperature of the system [1]. In general, a Fermi distribution describes numbers of particles, which obey the Pauli exclusion principle, occupying particular states and is described by

$$f(\varepsilon) = \frac{1}{e^{\frac{\varepsilon-\mu}{k_B T}} + 1} \tag{8}$$

where ε, μ, T are our particle energies, chemical potential and temperature and k_B is Boltzmann's constant. Given some particle density and temperature N and T we can compute our chemical potential

$$\mu = \frac{1}{\beta} \ln \left(e^{\hbar^2 N \beta \pi / m_r} - 1 \right) \tag{9}$$

and thus we can define a background or dynamic Fermi distribution with just those two parameters [1].

The electric field, $E(z,t)$ couples into these equations through the renormalized Rabi frequency

$$\Omega_k = \frac{d_{cv} E(z,t)}{\hbar} + \frac{1}{\hbar} \sum_{k \neq q} V_{|k-q|} p_q \tag{10}$$

where d_{cv} is a dipole transition element $\hbar$ is Planck's constant, and the single particle energy

$$\hbar\omega_k = \frac{\hbar^2\vec{k}^2}{2m_r} + E_g - \sum_{q\neq k} V_{|k-q|}(n_q^e + n_q^h) \tag{11}$$

where m_r and E_g are the reduced mass and band gap energy respectively. Note the nonlinear coupling done by the renormalization factor where $V_{|k-q|}$ is our screened potential matrix which describes the many-body Coulomb interactions in the semiconductor crystal lattice. In most simulations, those not containing the more fundamental scattering terms on the Second Borne-Markov level, this is the only nonlinear component and by far the most taxing component of the simulation. Additional terms include our spontaneous emission, modeled by

$$\Lambda_{spont}^{p(n)} = +(-)\Lambda_k^{spont} n_k^e n_k^h \tag{12}$$

with

$$\Lambda_k^{spont} = \frac{n_{bgr}^3}{\pi^2\varepsilon\hbar^4 c_0^3} |d_{cv}|^2 \left(\frac{\hbar^2\vec{k}^2}{2m_r} + E_g\right)^3 \tag{13}$$

for the background refractive index, n_{bgr} and material permittivity, ε [14]. Alternatively, in some situations, rather than letting spontaneous emission build up, one can introduce an initial pulse into the cavity to quicken the convergence of the simulation. This highly nonlinear coupled system of ODEs is a computational nightmare and it is where the predominant amount of computational time is spent during our simulations. As we push into transverse dimensions, discretizing our quantum wells in space, this becomes an even greater issue and many numerical techniques are required to reduce the computational demand of the simulations.

One implemented strategy is to only update the density dependent coulomb potential, $V_{|k-q|}$ and kinetic hole filling distribution, $F_k^{e(h)}$ when there is a significant amount of change in the electric field at the quantum wells. Similarly, when updating this matrix, instead of computing each element, we compute a few of the elements and interpolate between them to get the full matrix. Without strategies like this, this system would not be feasible.

Overall, many novel design techniques have been realized experimentally through the study of this model including a novel gain chip design for shorter pulses. Herein, we explore a small subset of those techniques, specifically those by Kilen et al in 2017 [20].

2.1 Ultrafast pulse generation strategies

Having described the relevant background, we proceed to a summary of the various strategies utilized to optimize pulse generation in optically pumped VECSEL cavities, as described by Kilen et al [20]. For the simulations in this paper, they use the phenomenological rate based scattering and dephasing terms rather than the full Second Borne-Markov approximations and start simulations from seed pulses rather than from spontaneous emissions. The cavity is set up similarly to Figure 1, except instead of using the typical resonant periodic gain (RPG) structure as is typical with VECSEL gain chips, they use the modified multiple quantum well (MQW) structure where all of the quantum wells are piled into a single antinode of the standing wave of the desired fundamental mode. The RPG structure positions the quantum wells at successive antinodes of the standing wave, thus ensuring maximum amplification of this mode. Piling all the QWs ona single antinode not only minimizes the dispersion by shortening this region, it all provides peak gain to a wider frequency band. This was shown to produce shorter, stronger pulses [1].

A partial list of simulation parameters is included in Table 1, where we indicate values for the SESAM (S) and gain chip (G) separately. All simulations were run on a SGI UV2000 shared memory computer, with implemented parallelization schemes, and could take upwards of $40hrs$ per simulation.

Description	Variable	Value
Kinetic hole filling rate	$\tau_{fill}^{S(G)}$	$100fs$
Central wavelength	ω_0	$980nm$
SESAM Carrier Density	n^S	$5.0e14\ cm^{-2}$
Gain chip Carrier Density	n^G	$3.25e16\ cm^{-2}$
Dephasing time (Estimated)	$\tau_{deph}^{S(G)}$	$50fs$
SESAM recovery rate	τ_{scat}^{S}	$2ps$
τ_{scat}^{G}	Gain chip recovery rate	$20ps$
Round trip time	RT	$21ps$
Background temperature	T_{bg}	$300K$
DBR pairs	-	30
DBR refractive indices	n_1, n_2	$1.9, 3.435$
AR coating refractive index	n_{AR}	1.72

Figures 2 and 3 show the round trip behavior of the inversion, highlighting the burning of a kinetic hole as a pulse comes in, then the recovery back to a quasi-Fermi distribution.

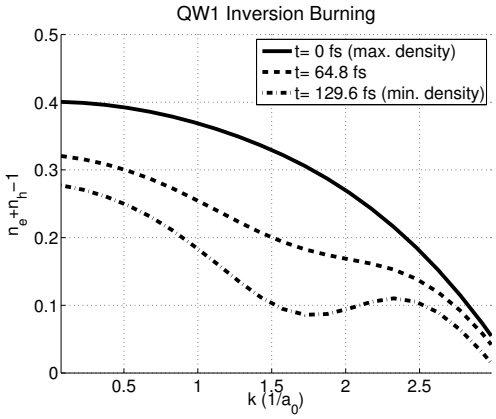

Figure 2: Inversion kin. hole burning

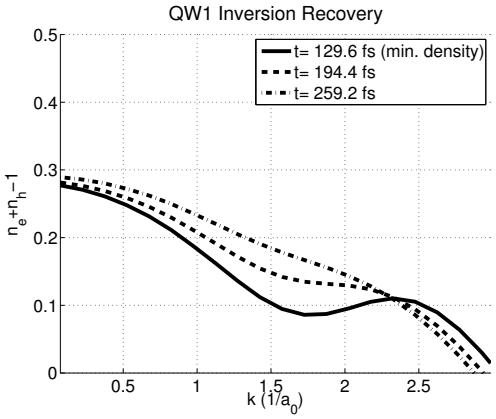

Figure 3: Inversion recovery

The configuration given by Table 1 resulted in an optimal modelocked pulse with a FWHM of $19fs$ and a peak intensity of $5.7MW/cm^2$. A narrowed DBR was also used, with a lower density $n^G = 2.9e16\ cm^{-2}$ resulting in a pulse FWHM of $46fs$ and a peak intensity of $1.7MW/cm^2$. The paper highlights the numerical equivalent of a pump probe experiment for finding the spectral gain, by using a low energy pulse passing in, then reflecting back out, through

the gain chip and comparing the result to the input,

$$Gain = \left| \frac{\hat{E}_{out}(\omega)}{\hat{E}_{in}(\omega)} \right| - 1 \tag{14}$$

for the Fourier transforms of the input and output pulse amplitudes. The paper illustrates how the gain is broadened and the Group Delay Dispersion (GDD) is flattened for the MQW over the RPG structure. The GDD is responsible for the spreading of the pulse and is flattened by optimizing over AR coatings for a given cavity setup. The flattening of the GDD, as well as the gain broadening, results in narrower pulses.

The paper also described an inherent hysteresis effect in the model that has been seen experimentally [21]. They first achieved a stable mode-locked pulse at a relatively high carrier density, $n^G = 4.0e16cm^{-2}$ then gradually decreased the density by $0.15e16cm^{-2}/ns$ and compared the results to full modelocking simulations at the various densities. They found that starting from a modelocked state, the system was able to stay modelocked even for densities below which no pulse could build up from noise, $n^G = 3.17e16\ cm^{-2}$. Although, the equilibrium gain is lower than the absorption, the pulse was able to obtain a different modelocked state. Having discussed some applications of this model, we can proceed to discuss our attempts at utilizing this model for future work.

3 Current and future work

3.1 Implementing the basic transverse model

There are many interesting effects relevant to VECSELs that are not realizable using a one dimensional model including higher order mode generation [22], self-modelocking [23, 24], and the ideas of PT symmetric gain regions [25–27]. This motivates the implementation of a transverse profile into the model. The primary complications with this model are the pulse propagation and diffraction and the transverse discretization of the Semiconductor Bloch Equations.

To handle the pulse propagation, we note that our primary area of concern is the massive air cavity. Within the very narrow gain chip and SESAM, our pulse will not diffract dramatically and thus a method analogous to the one dimensional model should be sufficient. This is definitely something that should be investigated more rigorously, however due to the computationally intensive nature of the propagation, we will initially restrict the model in this way. Contrarily, within the air cavity, we cannot neglect the diffraction and phase changes of our transverse profile as the reshaping will have dramatic effects on the resulting modelocked pulse. In our linear model, this presents an issue since we do not have a curved mirror to refocus the diffracting beam. Thus, we introduce a curved mirror inside the cavity. Based on a desired beam waist at our gain chip, w_0, wavelength, λ, magnification, m and first distance s_1 we can compute our focal length, f and second distance s_2 [28]. These computations are done using

$$f = \frac{m\lambda^2 s_1^2 + m\pi^2 w_0^4}{\lambda((\lambda^2 s_1^2 - \pi^2 m^2 w_0^4 + \pi^2 w_0^4)^{1/2} + \lambda m s_1)} \tag{15}$$

$$s_2 = f\left(\frac{\frac{s_1}{f} - 1}{\left(\frac{s_1}{f} - 1\right)^2 + \frac{w_0^4 \pi^2}{f_1^2 \lambda^2}} + 1\right) \tag{16}$$

The required condition for stability of our resonator cavity is that

$$C = \left|\frac{2s_1 s_2}{f^2} - 2s_1 + s_2 f + 1\right| < \frac{1}{2} \text{ [29]} \tag{17}$$

Because our cavity can become unstable near $C = \frac{1}{2}$ we choose s_1 so that we are far from this bound. Although we have performed preliminary studies on this, a more thorough study could be performed to rigorously optimize these cavity lengths for stability and pulse characteristics.

To propagate our pulse through the lens, we apply a phase mask, a complex radially dependent phase derived from the paraxial wave equation, to our profile u

$$\tilde{u} = ue^{\frac{-ik_0 r^2}{2f}} \tag{18}$$

for radius r and wavenumber $k_0 = 2\pi/\lambda$ [29]. To propagate through free space, we have to decide on a numerical propagation technique. Because we

are in a linear medium where our field dies at the boundaries, we can use a pseudo-spectral propagator to propagate our solution the entire span of the space in a single step. The general scheme for propagating a solution u is thus

$$\tilde{u} = FFT^{-1}\left(Propagator \cdot FFT(u)\right) \tag{19}$$

where our propagator is derived as a Green's function for the wave equation

$$Propagator = e^{iz\left(\sqrt{k_0^2 - k_x^2} - k0\right)} \tag{20}$$

for our Fourier space variable, and current wavenumber, k_x, and distance $z = s_{1,2}$ [30].

With our propagator thus defined, and the resulting modifications included in the C++ implementation, we have obtained our first modelocking results, shown in Figure 4. The top middle and bottom plots show the evolution of the total intensity, the peak intensity, and the FWHM in both time and space, respectively.

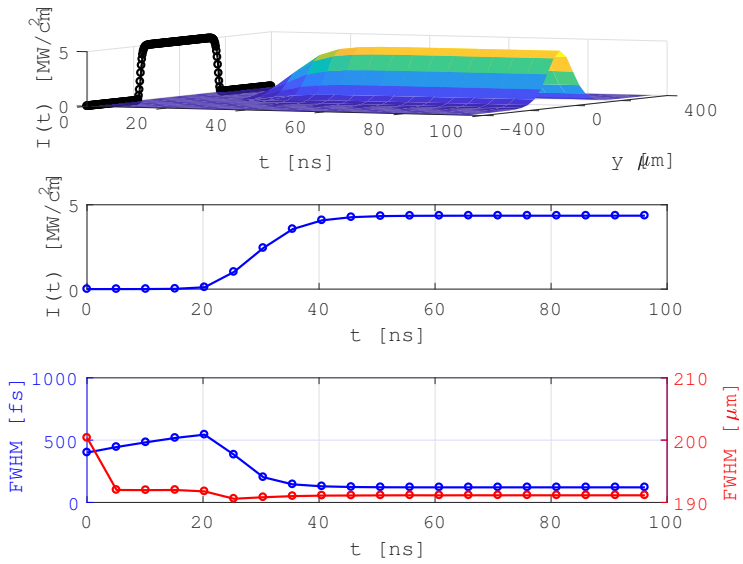

Figure 4: First modelocking sim.

The results show that our pulse stabilized after about $50ns$, equivalent to 2500 Round trips with a peak intensity about $4.8MW/cm^2$ and FWHM of $191\mu m$ and $150fs$ for space and time, respectively.

From here, we need to determine the appropriate resolution in the transverse dimension. The key consideration is that we ensure we have enough

points to properly resolve our fundamental Gaussian, and higher order modes, on both the gain chip and SESAM. Modeling a basic resonator cavity, we studied the accumulated errors at various magnifications, with respect to the number of points in our discretization. To ensure that we capture the full pulse, we used a domain size of $8 \cdot FWHM$ of our gain chip. In full simulations we zero-pad our domain so that the actual domain need not be this large and we assume it to be $4 \cdot FWHM$ to fully capture the pulse. The results are shown in Figures 5 and 6, for 1 round trip and 10000 round trips respectively. Therein, we are looking at the errors in our numerically propagated solutions compared to the analytic Gaussian solutions on the gain chip (LHS) and SESAM (RHS) respectively.

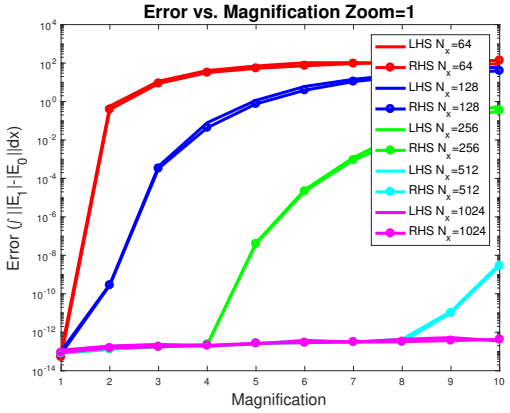

Figure 5: Errors after 1 Round-trip

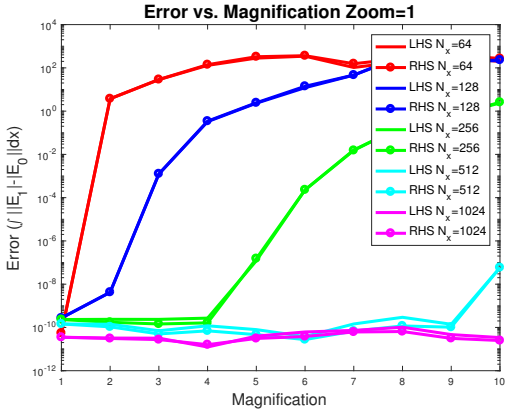

Figure 6: Errors after 10000 Round-trips

For $N_x = 1024$, we thus have a minimal error, which cannot be reduced by increasing the number of points. Because of the other errors inherent in our simulation, a relative error of 10^{-8} is very reasonable and thus, for this size domain we need a minimum of 256 or 512 points within our domain to ensure acceptable errors. Due to the zero-padding of the domain this reduces to 128 and 256. For efficient computations, we require that the number of points be an integer multiple of the number of threads per node on our SGI UV2000 shared memory computer and thus we use $N_x = 288$ for all simulations. When we have a weak magnification, $m \leqslant 4$, we can also use $N_x = 144$. A thorough study of the effect magnification has on our pulses is potentially interesting. In addition to the stability of our resonator, we also need to ensure that our final modelocked pulse is converged. Although there has been some preliminary work in this regard, a thorough study of the convergence

of our solutions still needs to be completed.

Potential complications that may arise concern when our cavity exhibits higher order modes with fine transverse features. A complete set of orthogonal modes for our resonator cavity are described by the Hermite-Gaussians [31].

The general form of these is given by Equation 21

$$u(x,z) = H\left(\frac{\sqrt{2}x}{w(z)}\right) e^{-\frac{x^2}{w(z)^2}} e^{i\frac{kx^2}{2R(z)}} e^{ikz+i\phi(z)} \tag{21}$$

wheren $H(x)$ are the Hermite polynomials, $R(z)$ is the current radius of our fundamental Gaussian solution, and $\phi(z)$ is the accumulate Guoy phase which distinguishes beam and pulse propagation from plane wave propagation [32].The order indicates the order andnumber of zero crossings of the Hermite polynomial. A selected few of these modes are shown in Figure 7.

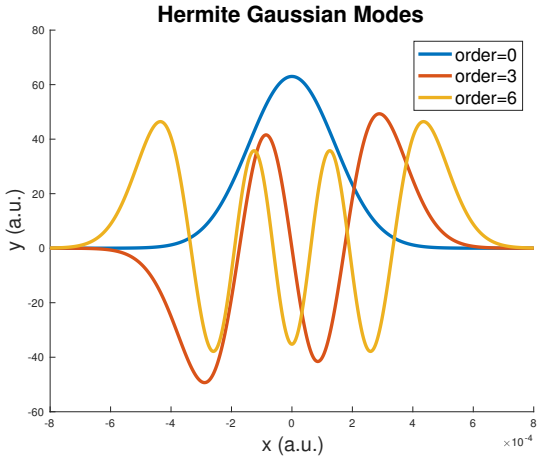

Figure 7: A set of Hermite Gaussian modes

We have already seen a superposition of these modes within our simulations when we used a large pump to mode size ratio, $R > 1.5$, an example of which is shown in Figure 8

We then have a new behavior where the relative phase of our modes flips on successive round trips so that we get a two round trip periodic behavior, with more energy concentrated towards the center versus the sides of the pump profile and then flipping on the next round trip. We also note that

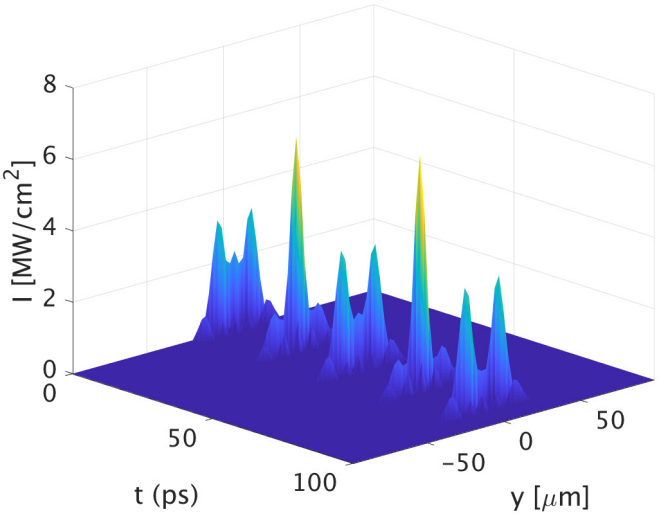

Figure 8: Wide pumping output after $145ns$

we do not have a single pulse but rather a pulse molecule. Figure 9 shows the temporal profile of this molecule, a similar profile to results obtained in the one dimensional model. Contrary to that model, Figure 10 shows that the weaker pulse of the molecule exhibits much higher transverse oscillations indicative of higher order modes. We make a quick note that these higher order modes have only a couple of points beneath each crest and thus we would not expect to be able to resolve modes of higher order than this one.

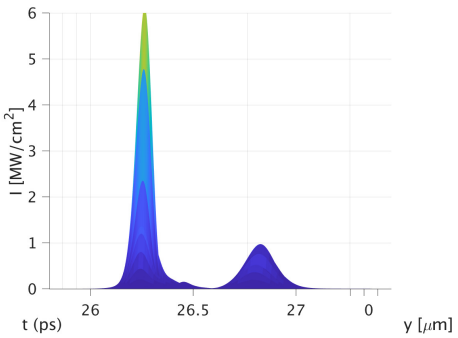

Figure 9: Side view of pulse molecule

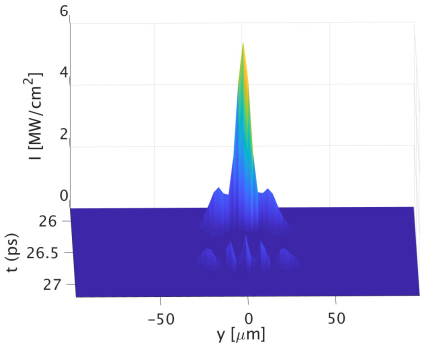

Figure 10: Front view of pulse molecule

It has been proposed that we could eliminate these modes by increasing the recovery rate for our carriers back to the background distribution. In addition, it has been suggested that we might be able to generate a complete set of these modes by systematically utilizing two separate pump profiles and

displacing them off-axis so that the peak gain is no longer centered over the origin but rather over the peaks of the desired higher order mode [22, 23]. Comprehensive studies of both of these phenomena are underway.

As shown, we currently have the transverse model generating modelocked pulses and are actively adding features to its capabilities. One goal is to examine the effect of cavity geometry on the pulse, through the introduction of varying cavity geometry and non-normal incidence on our gain chip and SESAM.

3.2 Studying cavity geometries

There exist many different, and interesting, VECSEL cavity geometries worth considering, a few of which are shown in Figure 11.

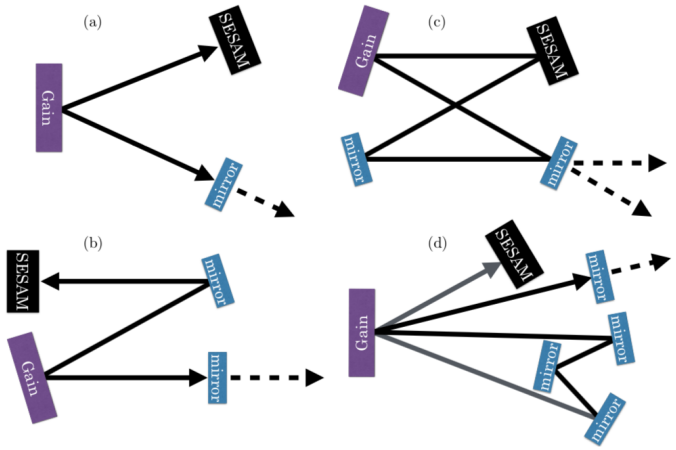

Figure 11: Various VECSEL cavity arrangements: V (a), Z(b), ring (c), and F(d) [2]

We can form even more complex geometries with multiple gain chips, or SESAMs, and ones that have counter-propagating pulses inside of them. One immediately interesting consequence of these non-linear cavities is the effect angle of incidence has on the resulting pulse. For example, in the V-cavity arrangement as shown, our pulse can be incident on our gain structure with a significant angle. This corresponds to a delay between when the wings of the pulse hit the structure. Specifically, for a given pulse width, w_0, the delay between the wings hitting the interface is computed as

$$\Delta t = \frac{w_0 \tan\theta}{c} \tag{22}$$

where θ is our angle of incidence and c is the speed of light within the medium, taken as a constant. For a $200\mu m$ wide beam at a modest angle of incidence $\theta = \pi/9$ this corresponds to a delay of about $243fs$. This can be much longer than our temporal FWHM and thus the front end of the pulse will have completely left the gain region by the time the back end enters it. This could result in much different pulses from what has been observed previously, both in the stable and unstable regime. This angle also introduces an increase in optical path length through the structure, and thus there will be increased dispersion of the pulse leading to different, more realistic pulse formation.

The main questions of concern when modeling these cavities is how to succinctly model the new geometry, how to account for the angle properly during free space propagation, and within the structure itself, as well as how to model the various incoming and outgoing fields within the structure. Regarding the additional mirrors and propagation distances, there exists a useful domain transformation using ABCD matrices. [29]. Generally, using ray optics we can model how individual rays are affected by various optical elements through the successive application of ABCD matrices. Given some ray with position y and angle θ then the effect of a linear optical element can be seen through the multiplication of the vector $(y\ \theta)$ by the appropriate ABCD matrix. Two important matrices are for a curved mirror with focus, f, given by Equation 23

$$\begin{bmatrix} 1 & 0 \\ -\frac{1}{f} & 1 \end{bmatrix} \tag{23}$$

and for free-space propagation of a set distance, L, given by Equation 24,

$$\begin{bmatrix} 1 & L \\ 0 & 1. \end{bmatrix} \tag{24}$$

Given some ABCD matrix, we can transform this matrix into an analogous cavity with two mirrors separated by free space, namely, as shown in Equation 25,

$$\begin{bmatrix} A & B \\ C & D \end{bmatrix} = \begin{bmatrix} 1 & 0 \\ -\frac{1}{f_1} & 1 \end{bmatrix} \begin{bmatrix} 1 & L \\ 0 & 1 \end{bmatrix} \cdot \begin{bmatrix} 1 & 0 \\ -\frac{1}{f_2} & 1 \end{bmatrix} \tag{25}$$

This simplifies to

$$L = B, \frac{1}{f_1} = \frac{B}{1-A}, \frac{1}{f_2} = \frac{B}{1-D} \tag{26}$$

Thus we can generalize diverse cavity domains to a simple three component cavity. What is even more appealing is that since our lens are merely a single flop per transverse point and we have eliminated oone of the more costly free-space propagations in our domain, propagation within this transformed domain is even faster to compute than our original domain for the linear cavity and does not change for more complex cavities. One caveat to this is that we still need to have the temporally resolved field that is incident on our quantum wells. As we saw previously, the angle of incidence on a gain structure, or SESAM, can impose a heavy delay on our pulse. The pseudo-spectral propagation method we are using readily extends to include this angle. We can enforce the time delay by looking backwards at previous steps of our pulse. Namely, using a modification to Equation 22, we can look appropriately far back for each transverse point. These points will not likely coincide with our exact temporal steps and so some interpolation is necessary. The obvious drawback to this is that we now need to store a large array of previous time steps for both the incoming and outgoing fields in either direction. The actual time delays as a function of distance and angle, are shown in Figure 12.

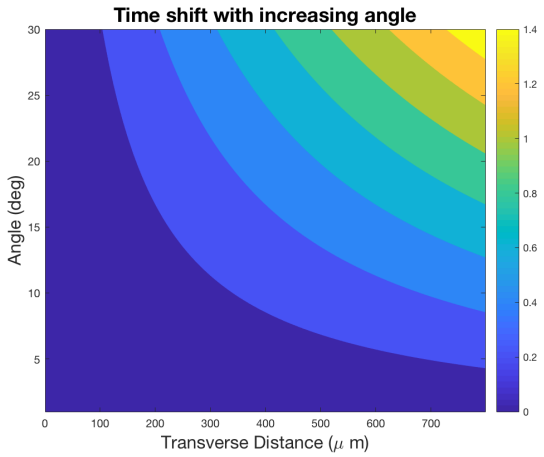

Figure 12: Time delay over relevant angles

Note that, even for the relatively small domain of $800\mu m$ we can have picosecond scale delays. In general our gain chips are shorter than $10\mu m$ with materials whose refractive indices are generally smaller than $n = 3.5$. Thus, a simple calculation reveals that our pulse spends less than $240fs$ inside the gain chip. Then for oblique angles, the pulse will interact with the quantum

wells in a much more complex fashion with potentially very interesting results.

An additional complication that arises at oblique angles is that along with a time delay, there will be an additional diffraction and phase accumulation for various portions of the pulse. Modeling this realistically with our spectral solver would require separate propagation distances for each point, resulting in an extra Fourier transform pair for each transverse point. To avoid this, we tested an alternate scheme, propagating the entire pulse the distance the midpoint traveled and compared this to the sequential propagation, described before.

Shown in Figure 13 is an initial beam propagated to a final distance, then sliced to model the pulse incidence on the interface. The top two panels show the initial and final pulse, from left to right, respectively. The bottom two panels show the single propagation distance and sequential propagation distances procedure as described. Figure 14 shows the amplitude and total error between these two procedures, a relative error peaking around 0.1%, which should be acceptable for our simulations.

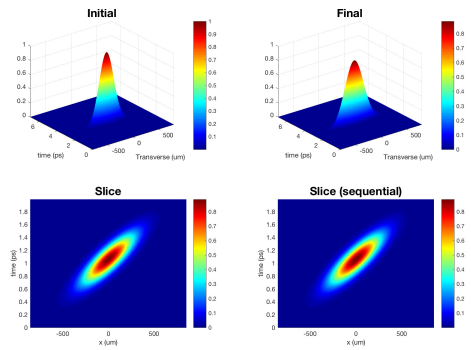

Figure 13: Comparison of propagation techniques

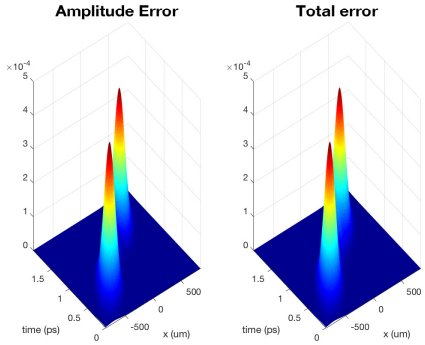

Figure 14: Error between propagation techniques

Thus, we can propagate a single distance along each leg without accumulating an excess of diffraction errors.

Another problem to overcome concerning the propagation within oblique incident cavities concerns how the field propagates within the narrow layers of the gain chip and SESAM structures. Since the fields do not interact except

at the quantum well interfaces, we can treat them separately and superimpose them at these interfaces. The key question is how to adequately propagate them within the structure and how to transfer them across the interface. Our approach is to model four separate fields at each point within the structure as evidenced in Figure 15. The four fields are made up of fields from the left (L) and right (R) path moving forward (+) and backward (-).

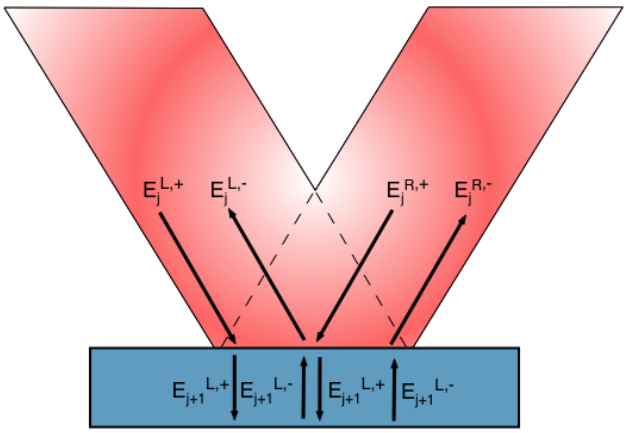

Figure 15: Field superposition inside gain chip (SESAM) structure

We ensure that for each structure, energy entering from one path, leaves from the other. We thus have a general transfer matrix

$$\begin{bmatrix} E_{j+1}^{L+} \\ E_{j}^{L-} \\ E_{j+1}^{R+} \\ E_{j}^{R-} \end{bmatrix} = \begin{bmatrix} \tau & \rho & 0 & 0 \\ 0 & \tau & \rho & 0 \\ 0 & 0 & \tau & \rho \\ \rho & 0 & 0 & \tau \end{bmatrix} \begin{bmatrix} E_{j}^{L+} \\ E_{j+1}^{L-} \\ E_{j}^{R+} \\ E_{j+1}^{R-} \end{bmatrix} \tag{27}$$

where ρ, τ are Fresnel reflection and transmission coefficients, respectively. If we assume TE polarized light, we have

$$\begin{aligned} \rho &= \frac{\cos\theta - \sqrt{\left(\frac{n_{j+1}}{n_j}\right)^2 - \sin^2\theta}}{\cos\theta + \sqrt{\left(\frac{n_{j+1}}{n_j}\right)^2 - \sin^2\theta}} \\ \tau &= 1 - \rho \end{aligned} \tag{28}$$

The immediate concern with this procedure is whether we are missing significant transverse motion within these structures. In the worst possible

case, we can test what would happen if we hit a low refractive index block, $n = 2$, longer than our longest structure, $L = 10\mu m$ at a highly oblique angle $\theta = \pi/6$. The angle of refraction is given by Snells law, Equation 29

$$n_1 \sin\theta_1 = n_2 \sin\theta_2. \tag{29}$$

Using this, we find that the maximum possible transverse shift is $\Delta x = 5\mu m$. This amounts to just a couple percent of our beam waist and less than 2 transverse grid points for even the most conservative domain discretizations. In a more realistic case, such as a structure similar to Figure 1, we will have a transverse shift less than $2.5\mu m$. This is well below a single transverse step size. Further, most of our field is reflected within the first half of the DBR and thus only a small portion of the field will actually experience this much shift. Most of the field will experience a far smaller shift. Thus, our model should accurately model this reflection. We plan to compare this to a full alternating direction implicit solver with coupled interface conditions to compare the true shift and ensure that it is bounded as calculated.

With each of these components, along with the proper implementation of a class structure in our full model, we thus have a general method for simulations of a general class of cavities.

3.3 Spontaneous (Self) Modelocking

There is a well known phenomenon in the study of lasers known as spontaneous, or self, modelocking (SML) in which the behavior of the beam itself causes modelocking rather than through the use of some active, or passive, modelocking device [23]. This has been shown previously in the study of VECSELs, [24, 33, 34]. The fundamental claim is that the Kerr-lens developed by the pulse's nonlinear interaction with the chip medium creates a focus as the pulse grows. By introducing an aperture into the cavity, we can introduce a high loss while the pulse is weak. If we tune this properly, the pulse peak can still grow, so that more of the pulse is focused within the aperture and thus the loss lowers until the pulse completely depletes the gain and the pulse can no longer maintain its growth. Thus, the loss takes over and the pulse shrinks. Through many round trips, this process is claimed to

stabilize into a sub-picosecond modelocked pulse [24].

These results are highly controversial and various groups claim that there is not enough evidence of stable modelocking [23, 35]. They observed the so-called SML but also observed fluctuations over microsecond time scales citing variations in temperature or pump power as possible causes. They argue that the given proof is insufficient.

Our goal is to provide a theoretical and numerical argument either for or against SML. In order to do this, the primary requirement is to enable a transversally and intensity dependent refractive index within our cavity components. This change will be modeled using Equation 30

$$n = n_{bg} + n_2 I \tag{30}$$

for our background refractive index, n_{bg}, our nonlinear refractive index, n_2 and our pulse intensity, I. We first would need to determine an appropriate value for n_2 or a different model for the refractive index of our material. As of right now, our propagation within the gain chip and SESAM structures is done through a careful tuning of our discretization steps with regards to our optical path lengths. Thus, a significant change in refractive index corresponds to a change in our discretization scheme. If this change is significant, this may require updating our scheme at each step. To do this, would require interpolating our field at these new points, introducing additional errors, as well as potentially significant computational time, into our simulation. Alternatively, we could begin with the finest reasonable grid resolution and use a modified propagator within our nonlinear cavity components. This too is feasible, though would require significant overhaul to the model. We aim to investigate these different methods within a simpler Matlab model for comparison and to determine which would be the easiest to implement.

3.4 PT Symmetry

The study of Hamiltonians has historically been restricted to Hermitian operators since Hermiticity ensures real eigenvalues. However, over the past twenty years, systems observing both parity and time symmetry have been

of great interest since they too can observe all real spectra and yet are non-Hermitian [36]. The parity and time operators P,T respectively acts on a wavefunction ψ according to Equation 31

$$\begin{aligned} P\psi(r,t) &= \psi(-r,t) \\ T\psi(r,t) &= \psi^*(r,-t) \end{aligned} \tag{31}$$

for variables r, t for space and time, respectively [27]. An operator is said to be PT-symmetric if

$$[PT, H] = 0. \tag{32}$$

Although these systems can be difficult to realize in quantum mechanical systems, they show great promise in various photonics devices [27, 37]. Specifically, these ideas were used to create a supersymmetric laser array which operated at high power in a fundamental mode by creating a so-called quantum well high loss superpartner to their laser array [25]. Further, Ahmed et al numerically modeled such a system designed to represent a Vertical Cavity Surface Emitting Laser (VCSEL), the internal cavity analog to a VECSEL [26]. To do this, they used a spatially modulated complex refractive index

$$U(x) = n_{re}\cos(|x| + \phi) - i\sin(|x| + \phi) \tag{33}$$

for various ϕ along with a complex Ginsburg-Landau type equation

$$\partial_t A(r,t) = \left(p - |A|^2\right) A + i\nabla_\perp^2 A(r,t) + iU(r)A(r,t). \tag{34}$$

Note that the period of modulation for their system was much lower than their initial condition beam waist. They showed this to have excellent mode focusing qualities for particular values of ϕ, n_{re}, n_{im}. We could improve upon this result by utilizing our more sophisticated model for the gain and absorption within our system. There are three primary hurdles to doing this, of increasing difficulty. First, we would need to implement a transversally modulated refractive index. Second, we need to modulate the gain and absorption in our cavity a systematic, periodic fashion. This could be done through a modulated density profile and should not be overly complicated. Third, and most difficult, we need to create such a modification that is physically justifiable. Although it would be interesting academically to get a modelocked pulse using this type of system for an arbitrary system, it would be much more useful to design one which can be realized experimentally. Thus, whatever refractive index and pump profiles we choose must be chosen based on

realistic pumping and crystal growth conditions. The particulars of this are still in need of a lot of research. However, surpassing these three hurdles, could provide incredibly useful insight into a new class of self-focusing effects in VECSELs and lasers in general.

3.5 Additional Considerations

One final area of interest is in a numerical study concerning the Semiconductor Bloch Equations themselves. Although they are often used for numerical modeling purposes, there is little literature on proper modeling practices for various implementations. Specifically, the 4th Order Runge-Kutta is used almost ubiquitously on these models. This multi-step numerical method is given by Equation 35.

$$\begin{aligned} k_1 &= hf\left(t_n, y_n\right), \\ k_2 &= hf\left(t_n + \frac{h}{2}, y_n + \frac{k_1}{2}\right), \\ k_3 &= hf\left(t_n + \frac{h}{2}, y_n + \frac{k_2}{2}\right), \\ k_4 &= hf\left(t_n + h, y_n + k_3\right), \\ y_{n+1} &= y_n + \frac{1}{6}(k_1 + 2k_2 + 2k_3 + k_4). \\ t_{n+1} &= t_n + h \end{aligned} \tag{35}$$

Although this is a powerful numerical method, this author could not find any justification for its almost ubiquitous usage. Further, there is no work. to this author's knowledge, on numerically studying these equations at various levels of approximation. The goal would be to determine the most appropriate solvers for accuracy and computational time for the uncoupled equations, the renormalized equations in the Hartree-Fock limit, and the two-band model with scattering terms approximated on the second Born-Markov level. It would also be useful to extend this to the multiband model but this would require a more significant investment to fully understand and implement this model. This is currently being worked on as part of a course requirement and is anticipated to be continued afterwards.

In addition to this, we also hope to create a stand-alone document which contains all relevant information necessary for understanding, running, and modifying the MSBE model so that future researchers can utilize in more readily.

4 Conclusion

Through this paper, we highlighted an understanding of the previous and ongoing efforts in modeling and optimizing the design of VECSELs through the coupling of Maxwell's wave equation to the Semiconductor Bloch Equations at various levels of approximations. We described relevant physical, optical, and mathematical background as well as presented some particular results from a recent publication concerning this model. We proceeded to discuss this author's current and future efforts in utilizing a higher dimensional transverse model to study higher order mode generation, pulse instabilities, cavity geometry and oblique angle considerations, self-modelocking, and PT symmetric systems, as well as to numerically study the Semiconductor Bloch Equations themselves. Through this work the author hopes to make significant contributions to the field of numerically modeling optical systems in pursuance of a doctoral degree in Applied Mathematics.

References

[1] Isak Kilen. *Non-equilibrium many-body influence on mode-locked Vertical External-Cavity Surface-Emitting Lasers*. PhD thesis, University of Arizona, 2017.

[2] Dr. Rudiger Paschotta. Vertical external-cavity surface-emitting lasers, May 2018.

[3] Elias Towe, Robert F. Leheny, and Andrew Yang. A Historical Perspective of the Development of the Vertical-External-Cavity Surface-Emitting Laser. *IEEE Journal on Selected Topics in Quantum Electronics*, 6(6):1458–1464, November/December 2000.

[4] A. C. Tropper, H. D. Foreman, A. Granache, K. G. Wilcox, and S. H. Hoogland. Vertical-external-cavity semiconductor lasers. *Journal of Physics D: Applied Physics*, 37:75–85, April 2004.

[5] Anne C. Tropper, Adrian H. Quarterman, and Keith G. Wilcox. Ultrafast Vertical-External-Cavity Surface-Emitting Lasers. In James J. Coleman, A. Catrina Bryce, and Chennupati Jagadish, editors, *Advances in Semiconductor Lasers*, volume 86, chapter 7. Elsevier Inc., 2012.

[6] M. Guina, A Rantamäki, and A. Härk"onen. Optically pumped VECSELs: review of technology and progress. *Journals of Physics D: Applied Physics*, August 2017.

[7] C. N. Böttge, J. Hader, I. Kilen, J. V. Moloney, and S. W. Koch. Ultrafast pulse amplification in mode-locked vertical external-cavity surface-emitting lasers. *Applied Physics Letters*, 105, 2014.

[8] Ursula Keller and Anne C. Tropper. Passively modelocked surface-emitting semiconductor lasers. *Physics Reports*, 2006.

[9] Oliver D. Sieber, Martian Hoffman, Valentin J. Wittwer, Mario Mangold, MAtthias Golling, Bauke W. TIlma, Thomas Südmeyer, and Ursula Keller. Experimentally verified pulse formation model for high-power femtosecond vecsels. *Applied Physics B: Lasers and Optics*, April 2013.

[10] Bauke W. Tilma, Mario Mangold, Christian A. Zaugg, Sandro M. Link, Dominik Waldburger, Alexander Klenner, Aline S. Mayer, Emilio Gini,

Matthias Golling, and Ursula Keller. Recent advances in ultrafast semiconductor disk lasers. *Light: Science & Applications*, 4(310), July 2015.

[11] Arash Rahimi-Iman. Recent advances in vecsels. *Journal of Optics*, 18, 2016.

[12] M Guina, A Rantamäki, and A Härkönen. Optically pumped vecsels: review of technology and progress optically pumped vecsels: review of technology and progress optically pumped vecsels: review of technology and progress. *Journal of Physics D: Applied Physics*, 50, 2017.

[13] Herman A. Haus. Mode-locking of lasers. *IEEE Journal on Selected Topics in Quantum Electronics*, 6(6):1173–1185, November 2000.

[14] Ada Bäumner, Stephan W. Koch, and Jerome V. Moloney. Non-equilibrium analysis of the two-color operation in semiconductor quantum-well lasers. *Physica Status Solidi B*, 248(4):843–846, September 2011.

[15] Sophocles J. Orfanidis. *Electromagnetic Waves and Antenna*. Rutgers University, 2016.

[16] Hartman Haug and Stephan W. Koch. *Quantum Theory of the Optical and Electronic Properties of Semiconductors*. Worl Scientific, 4 edition, 2004.

[17] Masud Mansuripur. *Field, Force, Energy and Momentum in Classical Electrodynamics*. Bentham Books, 2011.

[18] J. Hader, S. W. Koch, and J. V. Moloney. Microscopic theory of gain and spontaneous emission in GaInNAs laser material. *Solid State Electronics*, 47:513–521, 2003.

[19] I. Kilen, S. W. Koch, J. Hader, and J. V. Moloney. Fully microscopic modeling of mode locking in microcavity lasers. *Journal of the Optical Society of America B*, 33(1), December 2015.

[20] I. Kilen, S. W. Koch, J. Hader, and J.V. Moloney. Non-equilibrium ultrashort pulse generation and strategies in VECSELs. *Optica*, 4(4):412–417, April 2017.

[21] Dominik Waldburger, Sandro M. Link, Cesare G. E. Alfieri, Matthias Golling, and Ursula Keller. High-power 100-fs sesam-modelocked vescel. In 10087, editor, *Vertical External Cavity Surface Emitting Lasers (VECSELs) VII*. SPIE, 2017.

[22] Michal L. Lukowski, Jason T. Meyer, Chris Hessenius, Ewan M Wright, and Mahmoud Fallahi. Watt-level high order hermite-gaussian and laguerre-gaussian beams from vertical external cavity surface emitting lasers. *26th International Semiconductor Laser Conference, ISLC 2018*, pages 205–206, 2018.

[23] Mahmoud A. Gaafar, Arash Rahimi-Iman, Ksenia A. Fedorova, Wolfgang Stolz, Edik U. Rafailov, and Martin Koch. Mode-locked semiconductor disk lasers. *Advances in Optics and Photonics*, 8(3), September 2016.

[24] Mahmoud Gaafar, Philipp Richter, Hakan Keskin, Christoph Möller, Matthias Wichmann, Wolfgang Stolz, Arash Rahimi-Iman, and Martin Koch. Self-mode-locking semiconductor disk laser. *Optics Express*, 22(23), Novermber 2014.

[25] Mohammad P. Hokmabadi, Nicholas S. Nye, Ramy El-Ganainy, Demetrios N. Christodoulides, and Mercedeh Khajavikhan. Supersymmetric laser arrays. *Science*, 363(6427):623–626, February 2019.

[26] W. W. Ahmed, R. Herrero, M. Botey, and K. Staliunas. Locally parity-time-symmetric and globally parity-symmetric. *Physical Review A*, November 2016.

[27] Han Zhao and Liang Feng. Parity–time symmetric photonics. *National Science Review*, 5:183–199, January 2018.

[28] Sidney A. Self. Focusing of spherical gaussian beams. *Applied Optics*, 22(5):658–661, March 1983.

[29] Anthony E. Siegman. *Lasers*. University Science Books, 20 Edgehill Road, Mill Valley, California, 94941, 1986.

[30] Miroslave Kolesik. Opti 547: Beam propagation methods notes. Lecture notes part 2.

[31] E. G. Abramochkin and V. G. Volostnikov. Generalized gaussian beams. *Journal of Optics A: Pure and Applied Optics*, 6, March 2004.

[32] Peter W. Milonni and Joseph H. Eberly. *Laser Physics*. John Wiley and Sons, Inc., 2010.

[33] Y. F. Chen, Y. C. Lee, H. C. Liang, K. Y. Lin, K. W. Su, and K. F. Huang. Femtosecond high-power spontaneous mode-locked operation in vertical-external cavity surface-emitting laser with gigahertz oscillation. *OPTICS LETTERS*, 36(23):4581–4583, December 2011.

[34] Lukasz Kornaszewski, Gareth Maker, Graeme P.A. Malcolm, Mantas Butkus, Edik U. Rafailov, and Craig J. Hamilton. Sesam-free mode-locked semiconductor disk laser. *Laser and Photonics Reviews*, (6), 2012.

[35] J. V. Moloney, I. Kilen, A. Bäumner, M. Scheller, and S. W. Koch. Nonequilibrium and thermal effects in mode-locked VECSELs. *Optics Express*, 22(6):6422–6427, 2014.

[36] Carl M. Bender and Stefan Boettcher. Real spectra in non-hermitian hamiltonians having p t symmetry. *Physical Review Letters*, 80(24), June 1998.

[37] Vladimir V. Konotop, Jianke Yang, and Dmitry A. Zezyulin. Nonlinear waves in pt-symmetric systems. *Reviews of Modern Physics*, 88, 2016.